International Journal of Solids and Structures 51 (2014) 3931–3943

Contents lists available at ScienceDirect

International Journal of Solids and Structures

journal homepage: www.elsevier.com/locate/ijsolstr

Micromechanical analysis of friction anisotropy in rough elastic contacts

Stanisław Stupkiewicz [a,*], Maciej J. Lewandowski [a,b], Jakub Lengiewicz [a]

[a] Institute of Fundamental Technological Research (IPPT), Polish Academy of Sciences, Pawińskiego 5B, 02-106 Warsaw, Poland
[b] Faculty of Civil Engineering, Warsaw University of Technology, Al. Armii Ludowej 16, 00-637 Warsaw, Poland

ARTICLE INFO

Article history:
Received 3 March 2014
Received in revised form 30 June 2014
Available online 29 July 2014

Keywords:
Contact
Friction
Anisotropy
Roughness
Micromechanics

ABSTRACT

Computational contact homogenization approach is applied to study friction anisotropy resulting from asperity interaction in elastic contacts. Contact of rough surfaces with anisotropic roughness is considered with asperity contact at the micro scale being governed by the isotropic Coulomb friction model. Application of a micro-to-macro scale transition scheme yields a macroscopic friction model with orientation- and pressure-dependent macroscopic friction coefficient. The macroscopic slip rule is found to exhibit a weak non-associativity in the tangential plane, although the slip rule at the microscale is associated in the tangential plane. Counterintuitive effects are observed for compressible materials, in particular, for auxetic materials.

1. Introduction

Frictional response of a contact pair is called anisotropic when the friction coefficient, or more generally friction force or traction, depends on the direction of sliding. Anisotropic effects in friction are usually attributed to two sources: anisotropy of surface roughness or material anisotropy in a surface layer. This work is devoted to the micromechanical analysis of the former effect in elastic contacts.

Experimental evidence of friction anisotropy is very broad, some representative examples are mentioned below. Friction anisotropy has been observed in anisotropic materials such as crystals (Casey and Wilks, 1973; Hirano and Shinjo, 1993) and fiber-reinforced composite materials (Sung and Suh, 1979). Anisotropic roughness effects have been observed for textured surfaces (Zhang and Komvopoulos, 2009; Zhang et al., 2012), including contact of rubber-like materials (Konyukhov et al., 2008; Carbone et al., 2009; Ozaki et al., 2012) and biological contacts (Hazel et al., 1999; Murphy et al., 2007).

Macroscopic constitutive models of anisotropic friction are usually developed within the framework of plasticity theory (Michałowski and Mróz, 1978; Curnier, 1984; Mróz and Stupkiewicz, 1994; Konyukhov and Schweizerhof, 2006; Ozaki et al., 2012). Alternative approaches include the bi-potential method (Hjiaj et al., 2004) and friction-tensor description (Zmitrowicz, 1989). He and Curnier (1993) have introduced a friction model involving structural tensors that describe evolution of friction anisotropy resulting from relative motion of contacting bodies. Computational schemes for anisotropic frictional contact problems have been developed, for instance, by Hjiaj et al. (2004), Buczkowski and Kleiber (2006), Jones and Papadopoulos (2006) and Rodriguez-Tembleque and Abascal (2013).

In contrast to the macroscopic models mentioned above, micromechanical modeling approach considers interaction mechanisms at the microscale with the aim to provide a refined description of macroscopic properties and an improved understanding of physical phenomena. The general goal of micromechanics is to establish a link between macroscopic properties of materials, interfaces, etc., and their microscopic features, including microstructure and local interaction mechanisms. Classical applications of micromechanical modeling are concerned with heterogeneous bulk materials and their macroscopic bulk properties, and a variety of related approaches have been developed over the last decades, see, for instance, Nemat-Nasser and Hori (1999) and Qu and Cherkaoui (2006). However, the concepts of micromechanics can also be applied to interfaces. Contact interfaces, considered further in this work, are here typical examples, but other types of interfaces are also analyzed, for instance, microstructured interfaces at phase boundaries (Stupkiewicz et al., 2007; Petryk et al., 2010), imperfect or corrugated interfaces in composites (Bertoldi et al., 2007; Vinh and Tung, 2012; Quang et al., 2013), and others.

In the present context of contact of rough surfaces, the goal of micromechanical modeling is to predict macroscopic properties of a contact pair by considering interaction of surface asperities at the microscale. The macroscopic properties of interest may include, for instance, friction, contact compliance, real contact area fraction, thermal or electrical contact conductance, and wear.

* Corresponding author.
E-mail address: sstupkie@ippt.pan.pl (S. Stupkiewicz).

http://dx.doi.org/10.1016/j.ijsolstr.2014.07.013
0020-7683/

A popular approach for computing the overall contact response relies on a solution for a single asperity contact that is averaged over a distribution of asperity heights, radii, etc. That approach has been initiated by the pioneering work of Greenwood and Williamson (1966) and followed in numerous papers over the last decades. A related theory of Persson (2001) does not consider individual asperities but rather a spectrum of roughness length-scales and the corresponding length-scale distributions of contact pressure and real contact area fraction. Carbone et al. (2009) have extended that theory to anisotropic surface roughness with application to anisotropic rubber friction.

Computational contact homogenization is an alternative approach in which a microscopic boundary value problem is solved, typically using the finite element method, for a representative sample of rough contact interface, and macroscopic response is obtained by averaging the corresponding microscopic fields. The benefit of this approach is that geometrical and material nonlinearities, including arbitrary constitutive behavior of surface layers, can be directly included in the microscopic problem at the cost that the range of scales considered and spatial resolution are limited by the available computational resources. Related theoretical considerations within the framework of two-scale asymptotic expansions can be found in Orlik (2004) and Stupkiewicz (2007). Representative developments in computational contact homogenization include analysis of frictionless normal contact of hyperelastic and elastoplastic bodies (Bandeira et al., 2004; Pei et al., 2005), hysteretic effects in rubber contacts in the finite deformation regime (Wriggers and Reinelt, 2009; De Lorenzis and Wriggers, 2013), thermal contact conductance and thermomechanical contact (Varadi et al., 1996; Sadowski and Stupkiewicz, 2010b; Temizer, 2011), and third-body particles in contact interface (Temizer and Wriggers, 2008; Temizer and Wriggers, 2010). Interactions between the macroscopic deformation and the local deformation inhomogeneities at asperity contacts have been studied by Stupkiewicz (2007) and Sadowski and Stupkiewicz (2010a). Analysis of atomic-scale contact phenomena using molecular dynamics (MD) can be found in Anciaux and Molinari (2010) and Spijker et al. (2013).

Micromechanical modeling of friction anisotropy has attracted so far little attention. It seems that, apart from a recent model of rubber friction anisotropy (Carbone et al., 2009), the only micromechanical model of anisotropic friction is that developed by Mróz and Stupkiewicz (1994). In that model, one surface is represented by parallel rigid wedges, the other surface is represented by isotropically distributed asperities that may deform only in the normal direction (which corresponds to a Winkler foundation), and the contact interaction at the microscale is governed by the isotropic Coulomb friction model. Upon averaging, an orthotropic macroscopic friction model is obtained with the following three qualitative features:

(i) direction-dependent macroscopic friction coefficient is higher than the local friction coefficient;
(ii) friction is higher for sliding across the wedge-like asperities than for sliding along the wedges;
(iii) the macroscopic slip rule is not associated in the tangential plane.

Concerning the third property, we note that the local slip rule is associated in the tangential plane[1] and this associativity is not transmitted to the macroscopic friction model. This is in contrast to the classical micromechanics of heterogeneous materials, where the normality rule at the microscale is transmitted to the macroscale (Hill and Rice, 1973).

The present work has been directly inspired by the simple micromechanical model of Mróz and Stupkiewicz (1994). Our aim here is to apply the computational contact homogenization approach to study friction anisotropy resulting from asperity interaction in elastic contacts. Friction at local contacts is thus assumed to be the only dissipative mechanism in the system. Note that, in the model of Carbone et al. (2009), anisotropy of friction results from orientation-dependent hysteretic contribution due to viscoelastic deformation in a surface layer. Compared to the model of Mróz and Stupkiewicz (1994), more realistic surface roughness topographies are here considered, and asperity interaction is governed by a contact problem formulated for a deformable surface layer in the finite deformation regime. Micromechanical study of such a scope is carried out for the first time, to the best of the authors' knowledge.

The micro-to-macro transition procedure that is the basis of the adopted micromechanical framework can be regarded rather standard. Basic concepts concerning formulation of the microscopic problem, periodicity along the contact interface, boundary conditions and averaging rules are briefly introduced in Section 3, following Stupkiewicz (2007) and Temizer and Wriggers (2008). Section 4 is the main part of the paper and presents the results obtained for an idealized sinusoidal roughness as well as for randomly rough surfaces in relative sliding motion. It is shown that the three features (i)–(iii) of the micromechanical model of Mróz and Stupkiewicz (1994) are also observed in the present more general setting, but only for a nearly incompressible material. Quite surprisingly, properties (i) and (ii) do not hold for compressible hyperelastic materials and, in particular, for materials with negative Poisson's ratio (auxetics).

2. Orthotropic friction model

An orthotropic friction model is briefly introduced in this section as a reference for the micromechanical analysis of Section 4. Although a different notation is used in the presentation below, the model is fully equivalent to that proposed by Mróz and Stupkiewicz (1994). The model is a direct generalization of the classical isotropic Coulomb friction model, hence the friction coefficient and the slip potential are assumed independent of contact pressure.

Consider friction response of a contact pair that exhibits orthotropic symmetry. It is thus characterized by two friction coefficients $\mu_1 > 0$ and $\mu_2 > 0$ corresponding to the orthotropy axes specified by orthogonal unit vectors $\mathbf{e}_1$ and $\mathbf{e}_2$, respectively. Further, define the average friction coefficient μ as the geometric mean of μ_1 and μ_2 and parameter m characterizing the anisotropy according to

$$\mu = \sqrt{\mu_1 \mu_2}, \quad m = \sqrt{\frac{\mu_1}{\mu_2}}, \tag{1}$$

so that $\mu_1 = m\mu$ and $\mu_2 = \mu/m$.

An orthotropic friction condition can now be written in the following form,

$$\Phi = \|\mathbf{t}_T\|_{\mathbf{M}} - \mu t_N \leqslant 0, \quad \|\mathbf{t}_T\|_{\mathbf{M}} = \sqrt{t_{T\alpha} M^{\alpha\beta} t_{T\beta}}, \tag{2}$$

where $t_N \geqslant 0$ and $\mathbf{t}_T$ are, respectively, the normal and tangential components of the contact traction vector $\mathbf{t}$,

$$\mathbf{t} = -t_N \mathbf{n} + \mathbf{t}_T, \quad t_N = -\mathbf{t}\cdot\mathbf{n}, \quad \mathbf{t}_T = t_{T\alpha}\boldsymbol{\tau}^{\alpha}, \tag{3}$$

[1] By the associativity in the tangential plane, we mean that the slip velocity is normal to the section of the Coulomb cone by a plane of constant contact pressure. The local friction model obeys thus the normality rule in the tangential plane. Clearly, in the space of total contact tractions, the slip rule is not associated due to pressure dependence of the friction traction.

$\mathbf{n}$ is the unit normal to the contact surface, and $\boldsymbol{\tau}^\alpha$ is the tangent basis. $\|\cdot\|_{\mathbf{M}}$ denotes an elliptic norm defined by a symmetric, positive-definite tensor $\mathbf{M}$ that depends solely on parameter m. Specifically, in the Cartesian coordinate system aligned with the orthotropy axes, the components of tensor $\mathbf{M}$ are given by

$$M^{\alpha\beta} = \begin{bmatrix} 1/m^2 & 0 \\ 0 & m^2 \end{bmatrix}. \tag{4}$$

Assume further that frictional slip is governed by a slip potential Ψ so that the tangential slip velocity $\mathbf{v}_T$ obeys the following slip rule

$$\mathbf{v}_T = \dot\lambda \frac{\partial \Psi}{\partial \mathbf{t}}, \quad \dot\lambda \geqslant 0, \quad \dot\lambda \Phi = 0, \tag{5}$$

where the slip potential is assumed in the following form

$$\Psi = \|\mathbf{t}_T\|_{\mathbf{P}}, \quad P^{\alpha\beta} = \begin{bmatrix} 1/m^{2p} & 0 \\ 0 & m^{2p} \end{bmatrix}, \quad 0 \leqslant p \leqslant 1, \tag{6}$$

and the above components $P^{\alpha\beta}$ of tensor $\mathbf{P}$ correspond to the Cartesian coordinate system aligned with the orthotropy axes.

Parameter p scales the semi-axes of the ellipse defining the slip potential with respect to the semi-axes of the friction condition (2), thus Eq. (6) is in general a *non-associated* slip rule. Here and in the following, associativity or non-associativity of the slip rule refers to the tangent plane, i.e., to the section of the limit friction surface corresponding to a constant normal traction t_N. Considering the total contact traction $\mathbf{t}$, the slip rule (6) is, of course, not associated due to pressure-dependence of the friction traction, just like in case of the usual isotropic Coulomb friction model.

For $p = 1$, we have $\mathbf{P} = \mathbf{M}$ and the associated slip rule is obtained. For $p = 0$, the slip velocity $\mathbf{v}_T$ is coaxial with the friction traction $\mathbf{t}_T$. For $p = \frac{1}{2}$, the model of Zmitrowicz (1989) is obtained. Clearly, the isotropic Coulomb friction model is recovered for $\mu_1 = \mu_2$.

The above orthotropic friction model is illustrated in Fig. 1 which shows a section of the limit friction surface corresponding to a constant t_N. Angles α and β define the directions of the vectors of friction traction $\mathbf{t}_T$ and slip velocity $\mathbf{v}_T$, respectively, with respect to the orthotropy axis $\mathbf{e}_1$. The angle between the two vectors is denoted by δ,

$$\delta = \alpha - \beta. \tag{7}$$

Note that, according to this definition, the angle δ indicated in Fig. 1 is actually negative.

An alternative, more general description of anisotropic friction can be introduced using a polar representation of the friction traction $\mathbf{t}_T$. The friction condition and the slip potential are then expressed as

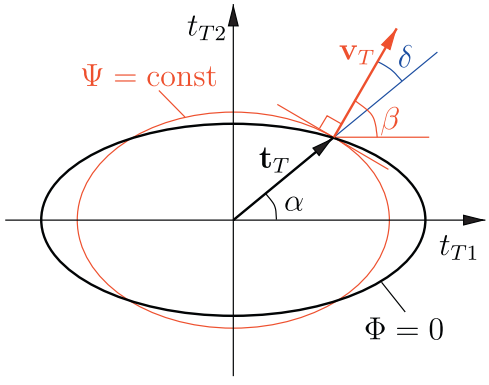

Fig. 1. Orthotropic friction model.

$$\tilde\Phi = \frac{\|\mathbf{t}_T\|}{f(\alpha)} - t_N \leqslant 0, \quad \tilde\Psi = \frac{\|\mathbf{t}_T\|}{g(\alpha)}, \tag{8}$$

where $f(\alpha)$ is the directional friction coefficient $\mu(\alpha) = \|\mathbf{t}_T\|/t_N = f(\alpha)$, and $g(\alpha)$ defines a convex slip potential. The slip rule (5) evaluated for the slip potential $\tilde\Psi$ yields

$$\mathbf{v}_T = \dot\lambda \frac{\partial \tilde\Psi}{\partial \mathbf{t}} = \frac{\dot\lambda}{g(\alpha)\|\mathbf{t}_T\|}\left(\mathbf{t}_T - \frac{g'(\alpha)}{g(\alpha)}\,\mathbf{n}\times\mathbf{t}_T\right), \tag{9}$$

from which the following simple expression for the angle δ is obtained (Mróz and Stupkiewicz, 1994),

$$\tan\delta = \frac{g'(\alpha)}{g(\alpha)}, \tag{10}$$

where $g'(\alpha)$ denotes the derivative of $g(\alpha)$. In case of the associated slip rule, we have $g(\alpha) = f(\alpha)$ and $\tan\delta = f'(\alpha)/f(\alpha)$.

3. Micromechanical framework

The goal of the present micromechanical analysis is to determine macroscopic (effective) friction properties of a contact pair in a relative sliding motion by considering surface roughness and asperity interactions. The scope of this work is restricted to *elastic contacts* so that the dissipation in the system is assumed to originate only from friction at the microscale, i.e., at local asperity contacts. Other dissipative mechanisms such as plasticity, viscoelasticity, thermal effects, etc., are not considered.

Assuming that the contacting bodies are elastic, the macroscopic friction properties depend only on surface roughness, which plays here the role of microstructure, and on the local friction model, which governs the contact interactions at the microscale. Real engineering surfaces are known to exhibit roughness on multiple scales, and fractal description is often adopted in that context, e.g., Majumdar and Bhushan (1991) and Persson (2001). In the approach adopted here, only a limited range of roughness length scales is explicitly considered due to the limitations imposed by the finite element discretization and by the associated computational cost. At the same time, contact at the microscale is assumed to be governed by the *isotropic Coulomb friction model*, and this can be interpreted to result from the asperity interactions at the lower scales that are not explicitly represented in the model.

In view of the specific assumptions adopted above, it is hard to identify a physically relevant system that would directly correspond to the considered class of problems. Rather, the aim of the present micromechanical analysis is to contribute to the basic understanding of the related phenomena and, in a broader perspective, to the development of micromechanical modeling approaches.

In the following, it is assumed that one of the bodies is rigid. Relaxing that assumption would not change much in the micromechanical framework, except that implementation would be somewhat more involved (and the computation time would increase). Clearly, the actual frictional response would probably be affected.

The macroscopic friction properties are obtained through a micromechanical testing procedure that is described below. The macroscopic friction traction $\bar{\mathbf{t}}_T$ is expected to depend on the macroscopic normal contact traction $\bar t_N$ and on the macroscopic slip velocity $\bar{\mathbf{v}}_T$. Actually, since a rate-independent friction model is assumed at the microscale, the macroscopic friction is also rate-independent, and only the orientation of $\bar{\mathbf{v}}_T$ matters, characterized by angle β, see Section 2. Here and below, the macroscopic quantities are denoted by a superimposed bar.

In principle, the micromechanical testing procedure amounts to solving a *microscopic problem* for prescribed control parameters $(\bar t_N, \beta)$, and the macroscopic friction traction $\bar{\mathbf{t}}_T$ is obtained by averaging the respective local fields. In practice, the microscopic

problem is formulated for a roughness sample of limited size so that representativeness of the sample cannot be guaranteed. As a remedy, several roughness samples can be analyzed, and the macroscopic response can then be obtained by averaging over an ensemble.

The main part of the micromechanical testing procedure is the solution of the microscopic problem. Following the ideas discussed in detail by Stupkiewicz (2007), see also Temizer and Wriggers (2008), the microscopic problem is formulated for a rough hyperelastic half-space that is brought to contact with a rough rigid surface of nominal normal $\bar{\mathbf{n}}$. The *periodicity* of the solution along the tangential direction is a necessary assumption that allows a consistent treatment of tangential friction stresses, see Stupkiewicz (2007). Accordingly, the half-space is fully represented by a periodic unit cell Ω, as illustrated in Fig. 2. The height of the cell in the direction normal to the nominal contact surface is selected such that the boundary conditions applied at the upper boundary Γ_l do not affect the solution up to a desired accuracy (Stupkiewicz, 2007; Temizer and Wriggers, 2008; De Lorenzis and Wriggers, 2013).

The assumption of periodicity implies that the roughness of both surfaces must also be periodic. This is schematically indicated in Fig. 2 where l denotes the period which is identical for both surfaces. An adequate notion of periodicity is also introduced for three-dimensional problems. Note that periodicity must be maintained in the deformed configuration which constrains the relative motion to be a translation, since a rotation about the normal direction would immediately break the periodicity. Also, the macroscopic in-plane deformation is not allowed as that would change the dimensions of the unit cell in the deformed current configuration.

The loading program applied in the microscopic problem consists of three phases:

(i) compression to a prescribed macroscopic normal contact traction $\bar{t}_N$ (or normal displacement $\bar{u}_N$) applied at the upper boundary Γ_l;
(ii) initial dragging at constant $\bar{t}_N$ (or $\bar{u}_N$);
(iii) the actual testing phase in which the unit cell is dragged at constant $\bar{t}_N$ (or $\bar{u}_N$) over the distance corresponding to the roughness period.

The purpose of the initial dragging phase (ii) is to erase the path-dependent effects associated with phase (i), so that the response in phase (iii) is truly periodic with respect to the time-like loading parameter.

The loading is applied at Γ_l, the upper boundary of the unit cell. Two types of boundary conditions can be considered: either a uniform normal traction (equal to $\bar{t}_N$) or a constant normal displacement $\bar{u}_N$ can be applied at Γ_l. In the latter case, the macroscopic normal contact traction is not known a priori – it is obtained as a part of the solution of the microscopic problem. In both cases, the lateral displacements at the upper boundary are fully prescribed.

Concerning the boundary conditions at the remaining part of the boundary, periodicity of the displacement is enforced on the lateral faces $\Gamma^{\pm}$ of the unit cell, which implies anti-periodicity of the corresponding tractions, and frictional contact with the rigid counter-surface is considered at the contact surface Γ_c which constitutes the bottom boundary of the unit cell.

The following weak form of the equilibrium equation constitutes the basis of the finite element implementation,

$$\int_{\Omega} \mathbf{S}\cdot\nabla\delta\mathbf{u}\,\mathrm{d}\Omega + \int_{\Gamma_l} \bar{t}_N\bar{\mathbf{n}}\cdot\delta\mathbf{u}\,\mathrm{d}\Gamma + \int_{\Gamma_c} (-t_N\delta g_N + \mathbf{t}_T\cdot\delta\mathbf{g}_T)\,\mathrm{d}\Gamma = 0, \tag{11}$$

where $\mathbf{S}$ is the first Piola–Kirchhoff stress, the displacement is periodic in the tangential plane, thus

$$\mathbf{u}(\mathbf{x}^+) = \mathbf{u}(\mathbf{x}^-), \quad \delta\mathbf{u}(\mathbf{x}^+) = \delta\mathbf{u}(\mathbf{x}^-), \tag{12}$$

where $\mathbf{x}^+ \in \Gamma^+$ and $\mathbf{x}^- \in \Gamma^-$ are two associated points on the lateral boundary of the unit cell, and the following boundary condition holds on Γ_l,

$$(\mathbf{I} - \bar{\mathbf{n}}\otimes\bar{\mathbf{n}})\mathbf{u}(\mathbf{x}) = \bar{\mathbf{u}}_T \quad \text{for } \mathbf{x}\in\Gamma_l, \tag{13}$$

where $\bar{\mathbf{u}}_T$ is a prescribed time-dependent tangential displacement, $\bar{\mathbf{u}}_T\cdot\bar{\mathbf{n}} = 0$. If the normal displacement $\bar{u}_N$ is prescribed on Γ_l instead of the normal traction $\bar{t}_N$, then the second integral in Eq. (11) vanishes, and the boundary condition (13) is replaced by the condition $\mathbf{u} = \bar{u}_N\mathbf{n} + \bar{\mathbf{u}}_T$ on Γ_l.

The third integral in the weak form (11) describes the contact contribution at Γ_c. The adopted finite-deformation contact formulation is standard; the details can be found in the monographs (Laursen, 2002; Wriggers, 2006). The contact kinematics is based on the closest-point projection with the deformable surface Γ_c being the slave surface. The inequality constraints resulting from unilateral contact and isotropic Coulomb friction conditions are enforced using the augmented Lagrangian method (Alart and Curnier, 1991; Pietrzak and Curnier, 1999). The details of the present contact implementation can be found in Lengiewicz et al. (2011).

The hyperelastic material model, used in this work, is specified by the following neo-Hookean-type elastic strain energy function,

$$\mathbf{S} = \frac{\partial W}{\partial \mathbf{F}}, \quad W(\mathbf{F}) = \frac{1}{2}\mu_e(\mathrm{tr}\,\bar{\mathbf{b}} - 3) + \frac{1}{4}\kappa_e(\det\mathbf{b} - 1 - \log(\det\mathbf{b})), \tag{14}$$

where $\mathbf{F}$ is the deformation gradient, $\mathbf{b}$ is the Finger deformation tensor, $\bar{\mathbf{b}}$ is its isochoric part,

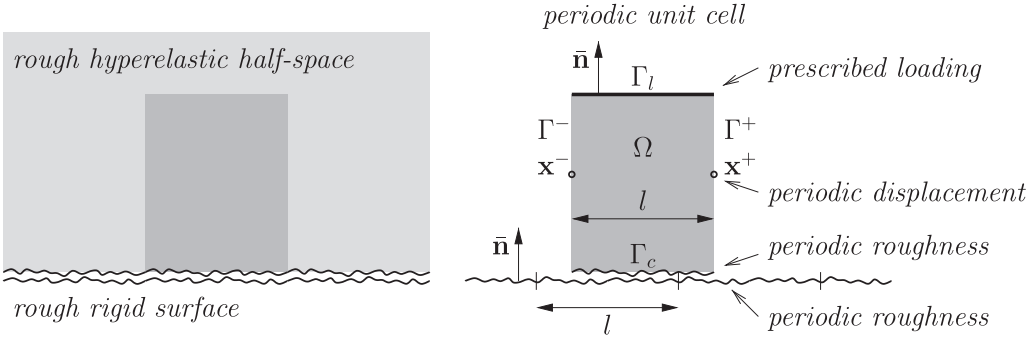

Fig. 2. Periodic unit cell used in the micromechanical testing procedure.

$$\mathbf{b} = \mathbf{F}\mathbf{F}^{\mathrm{T}}, \quad \bar{\mathbf{b}} = (\det \mathbf{b})^{-1/3}\mathbf{b}, \tag{15}$$

and the elastic shear modulus μ_e and bulk modulus κ_e are related to the Young's modulus E and Poisson's ratio ν by the usual relationships $\mu_e = \frac{1}{2}E/(1+\nu)$ and $\kappa_e = \frac{1}{3}E/(1-2\nu)$.

The macroscopic tangential contact traction $\bar{\mathbf{t}}_T$ and, if applicable, the macroscopic normal contact traction $\bar{t}_N$ are obtained by averaging of the local traction $\mathbf{t}$ at the upper boundary Γ_l according to

$$\bar{\mathbf{t}} = \frac{1}{\Delta t}\int_{t_0}^{t_0+\Delta t} \langle \mathbf{t} \rangle_{\Gamma_l} \mathrm{d}t, \quad \langle \mathbf{t} \rangle_{\Gamma_l} = \frac{1}{|\Gamma_l|}\int_{\Gamma_l} \mathbf{S}\bar{\mathbf{n}} \mathrm{d}\Gamma. \tag{16}$$

Here, the averaging involves *spatial averaging* over the upper boundary Γ_l and *time averaging* over the time period Δt corresponding to phase (iii). Additionally, *ensemble averaging* over several realizations (samples) of surface roughness is necessary if the roughness sample is not representative. Finally, the macroscopic friction coefficient $\bar{\mu}$ and angle α characterizing the orientation of the friction traction are given by

$$\bar{\mu} = \frac{\|\bar{\mathbf{t}}_T\|}{\bar{t}_N}, \quad \alpha = \arctan\frac{\bar{t}_{T2}}{\bar{t}_{T1}}. \tag{17}$$

Note that $\bar{\mu}$ and α may, in general, depend on both $\bar{t}_N$ and β.

Considering that the isotropic Coulomb friction is assumed at local contacts and that local friction is the only dissipative mechanism in the system, the macroscopic friction is expected to be affected by surface roughness only in the finite deformation regime, i.e., when the effects of non-zero asperity slope effectively appear.

4. Anisotropic friction effects in rough elastic contacts

4.1. Sinusoidal rigid surface

In this section, a detailed micromechanical analysis of anisotropic friction effects is carried out for the case of contact of a smooth hyperelastic half-space with a rigid sinusoidal surface. This is possibly the simplest configuration that features anisotropic (actually orthotropic) roughness and is thus expected to exhibit friction anisotropy at the macroscale. More realistic roughness is considered in the subsequent sections.

The sinusoidal rigid surface with a period l along the x-direction and an amplitude $2h$ is defined by the following equation

$$z(x,y) = z_0 + h\cos(2\pi x/l). \tag{18}$$

The roughness profile does not depend on the y-coordinate so that the microscopic problem is effectively two-dimensional, i.e., all unknowns depend only on x- and z-coordinates. However, the out-of-plane y-displacements are fully accounted for, and the problem is formulated as a *generalized plane strain* problem.

Further, the deformable surface is smooth, i.e., planar in the undeformed reference configuration. The microscopic problem can thus be formulated as a steady-state problem in an Eulerian frame attached to the rigid surface. Accordingly, the time averaging in the averaging rule (16) is omitted, and only the spacial averaging is applied to determine the macroscopic tangential contact traction (while the normal contact traction is prescribed). Since the material is hyperelastic, the solid part in the microscopic problem is not affected by the adopted Eulerian steady-state formulation. A non-standard treatment is only needed in the contact part when defining the slip velocity at the local contacts. Specifically, in steady-state conditions, the slip velocity $\mathbf{v}_T$ is given by the following relationship

$$\mathbf{v}_T = \mathbf{F}\bar{\mathbf{v}}_T, \tag{19}$$

where $\mathbf{F}$ is the deformation gradient and $\bar{\mathbf{v}}_T$ is the macroscopic slip velocity, i.e., the constant velocity of material points with respect to the fixed Eulerian frame in the undeformed reference configuration. Actually, only the tangential part of the deformation gradient $\mathbf{F}$ affects $\mathbf{v}_T$ which can thus be computed using surface data only.

The computations have been carried out for the asperity height h/l equal to 0.025, 0.05, 0.075 and 0.1, the local friction coefficient μ_0 equal to 0.1, 0.2 and 0.3, and the Poisson's ratio ν equal to $-0.8, -0.4$, 0, 0.25 and 0.45.[2] The value of the Young's modulus E may be left unspecified because the contact tractions are reported below only as the dimensionless tractions normalized by the reduced Young's modulus $E^* = E/(1-\nu^2)$.

In the finite-element implementation, four-node quadrilateral elements employing the F-bar formulation (de Souza Neto et al., 1996) are used for the solid part. Displacement periodicity (12) is enforced using the Lagrange multiplier technique, and the augmented Lagrangian method (Alart and Curnier, 1991; Pietrzak and Curnier, 1999) is used to enforce contact constraints. Computer implementation and finite-element computations are carried out using the *AceGen*/*AceFEM* system (Korelc, 2002, 2009), see also Lengiewicz et al. (2011) for the details of the present implementation of contact.

Fig. 3 shows the undeformed finite element mesh of the unit cell, as well as the deformed mesh for the case of the macroscopic slip velocity perpendicular to the sinusoidal wedges of the rigid surface, $\beta = 0$, for $h/l = 0.1$ and $\nu = 0.45$. The deformation pattern is further illustrated in Fig. 4, which shows the deformed mesh corresponding to the macroscopic slip velocity inclined with respect to the sinusoidal wedges. The color map in Fig. 4 shows the out-of-plane y-displacement which is otherwise not seen in the in-plane mesh deformation.

Note that a coarse mesh is shown in Figs. 3 and 4. The actual computations have been performed using a much finer mesh with element size reduced four times (and in some cases even eight times) with respect that shown in Figs. 3 and 4. In fact, a careful mesh convergence study has been performed, and a sufficiently fine mesh has been used so that the reported results are not visibly affected by the finite-element discretization.

The deformation pattern illustrated in Figs. 3 and 4 consists of overall shear (and compression) of the surface layer with a superimposed inhomogeneity due to contact with asperities. The associated distortion of the unit cell, and thus also the distortion of the individual finite elements, increases with increasing macroscopic friction traction, and this limits the range of contact pressures that can be simulated.

Results obtained for $\mu_0 = 0.2$ and $\nu = 0.45$ are summarized in Fig. 5. Anisotropy and pressure-dependence of the macroscopic friction coefficient are clearly seen in the polar plots of $\bar{\mu}(\alpha)$ shown in Fig. 5(a). The resulting orthotropic friction condition can be well approximated by the elliptic friction condition (2). It has been checked that the error of this approximation is below 1% in all cases that have been studied.

The markers in Fig. 5(a) denote the friction coefficients corresponding to the inclination angle β incremented by 10 degrees (in the computations, angle β has been incremented by 2.5 degrees). The non-radial placement of the markers corresponding to different contact pressures indicates that the macroscopic slip rule is also pressure-dependent. The macroscopic slip rule is further discussed at the end of this section.

[2] The negative Poisson's ratio ν, i.e., the auxetic behavior, is obtained in practice by microstructuring the material. In the present micromechanical framework, it is assumed that the material is homogeneous at the scale of asperities, which is not expected to hold for the known auxetic materials. In spite of that, the negative values of the Poisson's ratio ν are included in the analysis for completeness.

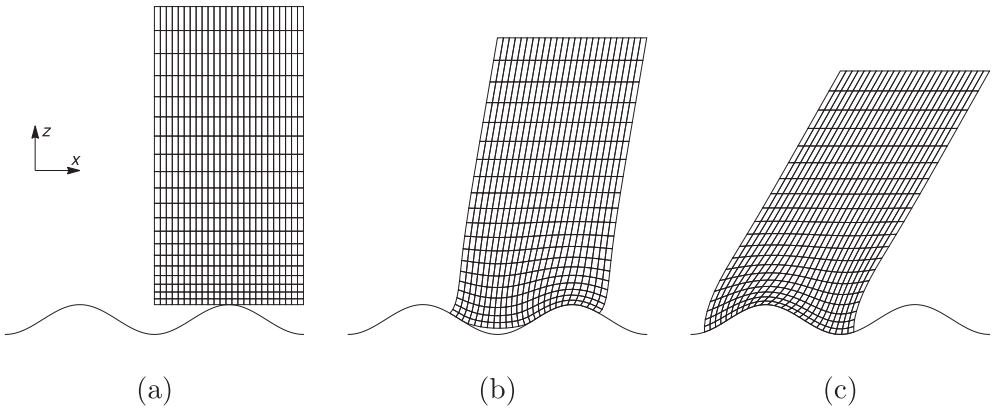

Fig. 3. Sinusoidal rigid surface: (a) undeformed mesh, (b) deformed mesh at $\bar{t}_N/E^* = 0.2$, (c) deformed mesh at $\bar{t}_N/E^* = 0.6$. Macroscopic slip velocity is perpendicular to the sinusoidal wedges ($\beta = 0$). A much finer mesh is used in the actual computations (see text).

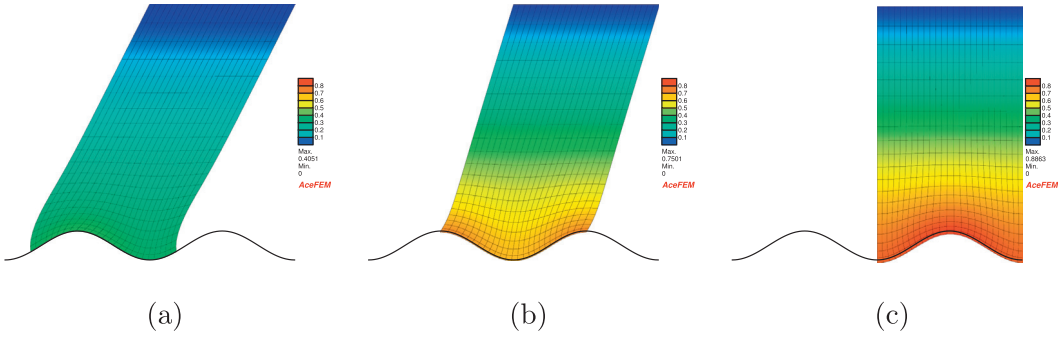

Fig. 4. Deformed mesh corresponding to the macroscopic slip velocity inclined at (a) $\beta = 30^\circ$, (b) $\beta = 60^\circ$, (c) $\beta = 90^\circ$ to the sinusoidal wedges at $\bar{t}_N/E^* = 0.6$. The color map shows the out-of-plane displacement u_y/l. A much finer mesh is used in the actual computations (see text). (For interpretation of the references to colour in this figure legend, the reader is referred to the web version of this article.)

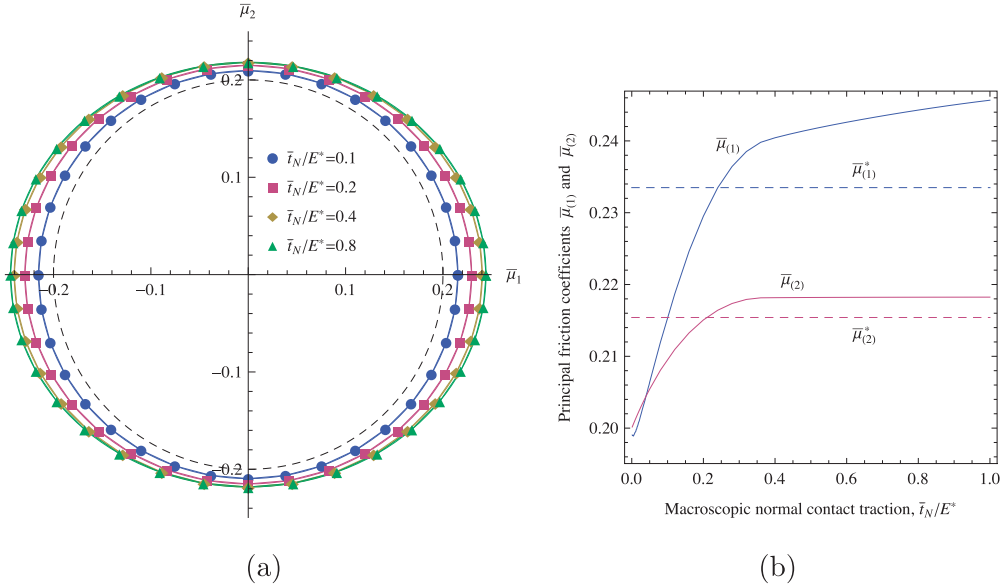

Fig. 5. Orientation- and pressure-dependence of the macroscopic friction coefficient for nearly incompressible material ($\nu = 0.45$): (a) polar plots $\bar{\mu}(\alpha)$ corresponding to selected values of macroscopic contact pressure $\bar{t}_N/E^*$; (b) principal friction coefficients $\bar{\mu}_{(1)}$ and $\bar{\mu}_{(2)}$ as a function of contact pressure $\bar{t}_N/E^*$. The dashed circle in figure (a) corresponds to the isotropic local friction coefficient $\mu_0 = 0.2$.

Sinusoidal roughness implies orthotropic symmetry of the macroscopic friction coefficient, and two principal friction coefficients can be defined: $\bar{\mu}_{(1)}$ and $\bar{\mu}_{(2)}$ corresponding to macroscopic slip velocity, respectively, perpendicular ($\beta = 0$) and parallel ($\beta = 90^\circ$) to the sinusoidal wedges. The principal friction coefficients $\bar{\mu}_{(1)}$ and $\bar{\mu}_{(2)}$ are shown in Fig. 5(b) as a function of the dimensionless macroscopic normal contact traction $\bar{t}_N/E^*$.

As a reference, the principal friction coefficients are compared to those predicted by the simple micromechanical model of Mróz and Stupkiewicz (1994). The latter are indicated by two dashed lines in Fig. 5(b), while their values are given by the following analytical formulae derived by Mróz and Stupkiewicz (1994),

$$\bar{\mu}^*_{(1)} = \frac{\mu_0}{1-(1+\mu_0^2)\sin^2\varphi}, \quad \bar{\mu}^*_{(2)} = \frac{\mu_0}{\cos\varphi}, \quad \bar{\mu}^*_{(1)} > \bar{\mu}^*_{(2)} > \mu_0, \tag{20}$$

where φ denotes the inclination angle of the wedge-like asperities considered in the simple micromechanical model, μ_0 is the local friction coefficient, and the inequalities in $(20)_3$ hold for $\varphi > 0$ and $\mu_0 > 0$. The values of $\bar{\mu}^*_{(1)}$ and $\bar{\mu}^*_{(2)}$ shown in Fig. 5(b) correspond to the average asperity slope of the sinusoidal wedges considered in the present work, i.e., $\varphi = \arctan(4h/l)$.

Three general features of the macroscopic friction model resulting from the present micromechanical analysis can be observed in Fig. 5. Firstly, surface roughness results in an increase of the macroscopic friction coefficient with respect to the local friction coefficient μ_0 (a dashed circle corresponding to the isotropic local friction model is included in Fig. 5(a)). Further, sliding across the sinusoidal wedges results in a higher friction than sliding along the wedges, i.e., $\bar{\mu}_{(1)} > \bar{\mu}_{(2)}$. Finally, the macroscopic friction coefficient increases with increasing contact pressure. The first two features are in a qualitative agreement with the micromechanical model of Mróz and Stupkiewicz (1994), see Eq. $(20)_3$.

Note, however, that the three effects mentioned above are reversed at very low contact pressures. For instance, it is seen in Fig. 5(b) that $\bar{\mu}_{(1)} < \mu_0$ for $\bar{t}_N/E^* < 0.02$, and $\bar{\mu}_{(1)} < \bar{\mu}_{(2)}$ for $\bar{t}_N/E^* < 0.05$. This has been found quite unexpected, and a detailed study of the corresponding effects has been carried out in order to confirm and understand those effects.

As illustrated and discussed in more detail later, the unexpected effects mentioned above have been found to be related to elastic compressibility of the material. Indeed, the results analogous to those presented in Fig. 5 for a nearly incompressible material ($\nu = 0.45$), but corresponding to an auxetic material with $\nu = -0.8$, exhibit similar qualitative features which are, however, much more pronounced, see Fig. 6. The principal macroscopic friction coefficient $\bar{\mu}_{(1)}$ across the sinusoidal wedges is now significantly lower than both the principal macroscopic friction coefficient $\bar{\mu}_{(2)}$ along the wedges and the local friction coefficient μ_0, and this occurs in a wide range of contact pressures.

The effect of elastic compressibility on friction anisotropy is further illustrated in Fig. 7 which shows the ratio of the principal friction coefficients, $\bar{\mu}_{(1)}/\bar{\mu}_{(2)}$, as a function of the contact pressure $\bar{t}_N/E^*$. The solid and dashed lines in Fig. 7 correspond to $\mu_0 = 0.3$ and $\mu_0 = 0.1$, respectively, while the results corresponding to $\mu_0 = 0.2$ (not shown) are in between. The effect of the local friction coefficient μ_0 on the anisotropy ratio is not much pronounced. The black dotted lines in Fig. 7 indicate the ratio $\bar{\mu}^*_{(1)}/\bar{\mu}^*_{(2)}$ resulting from Eq. (20) for $\mu_0 = 0.3$.

As shown in Fig. 7, the anisotropy ratio $\bar{\mu}_{(1)}/\bar{\mu}_{(2)}$ decreases with decreasing Poisson's ratio ν. Further, for all Poisson's ratios, there is a range of contact pressures for which $\bar{\mu}_{(1)}/\bar{\mu}_{(2)} < 1$, so that the friction coefficient across the sinusoidal wedges is lower than that along the wedges, and the corresponding range of contact pressures increases with decreasing Poisson's ratio. For a nearly incompressible material ($\nu = 0.45$), the corresponding range of pressures is relatively small but it significantly increases with decreasing Poisson's ratio.

The effect of the Poisson's ratio on the principal macroscopic friction coefficient $\bar{\mu}_{(1)}$ (sliding across the wedges) normalized by the local friction coefficient μ_0 is illustrated in Fig. 8. It is seen that $\bar{\mu}_{(1)}$ is lower than μ_0 for some range of applied macroscopic contact pressures, and that range increases with decreasing Poisson's ratio. This confirms the counterintuitive effect already illustrated in Figs. 5 and 6, namely that surface roughness may lead to *reduction* of friction in rough elastic contacts. This effect is clearly visible for a compressible material with $\nu = 0.25$, and it is even more pronounced for lower values of ν. Also, higher roughness (i.e., increased asperity height) results in a higher reduction of $\bar{\mu}_{(1)}$, compare Fig. 8(a) and Fig. 8(b).

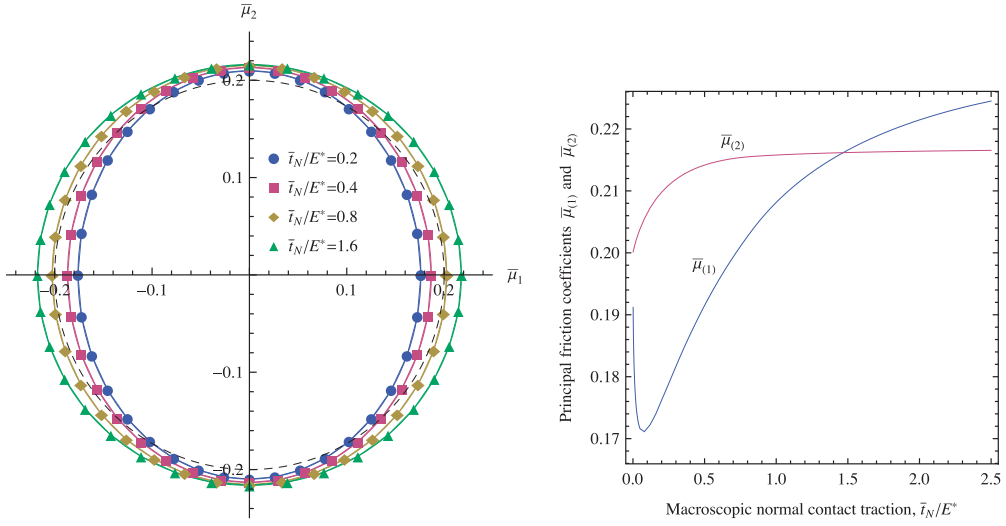

(a) (b)

Fig. 6. Orientation- and pressure-dependence of the macroscopic friction coefficient for compressible material ($\nu = -0.8$): (a) polar plots $\bar{\mu}(\alpha)$ corresponding to selected values of macroscopic contact pressure $\bar{t}_N/E^*$; (b) principal friction coefficients $\bar{\mu}_{(1)}$ and $\bar{\mu}_{(2)}$ as a function of contact pressure $\bar{t}_N/E^*$. The dashed circle in figure (a) corresponds to the isotropic local friction coefficient $\mu_0 = 0.2$.

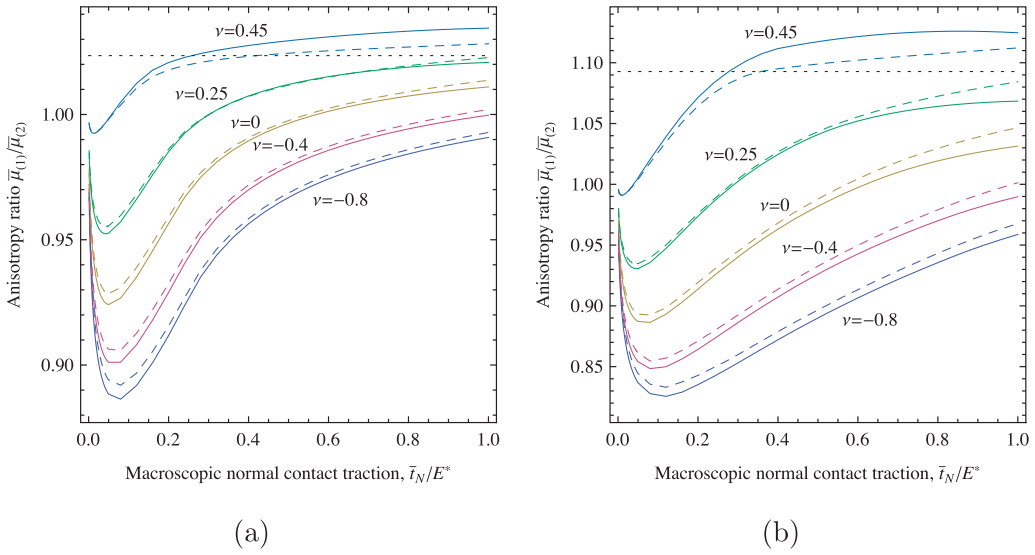

Fig. 7. Anisotropy ratio $\bar{\mu}_{(1)}/\bar{\mu}_{(2)}$ as a function of dimensionless normal contact traction $\bar{t}_N/E^*$ for: (a) $h/l = 0.05$, (b) $h/l = 0.1$. Solid and dashed lines correspond to $\mu_0 = 0.3$ and $\mu_0 = 0.1$, respectively.

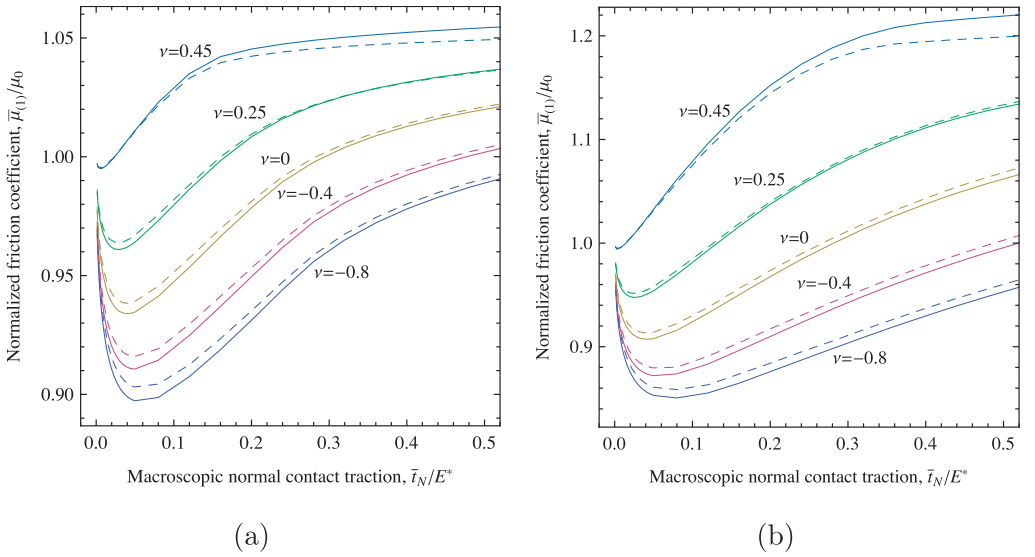

Fig. 8. Normalized principal macroscopic friction coefficient $\bar{\mu}_{(1)}/\mu_0$ as a function of dimensionless normal contact traction $\bar{t}_N/E^*$ for: (a) $h/l = 0.05$, (b) $h/l = 0.1$. Solid and dashed lines correspond to $\mu_0 = 0.3$ and $\mu_0 = 0.1$, respectively.

The effect of asperity height h/l is further illustrated in Fig. 9 where the principal friction coefficients $\bar{\mu}_{(1)}$ and $\bar{\mu}_{(2)}$ are shown for a representative case of $\nu = 0$. As expected, higher roughness results in higher friction, except at low pressures where $\bar{\mu}_{(1)}$ is reduced with respect to μ_0, and here higher roughness results in higher reduction of friction.

From Figs. 7–9, it follows that surface roughness influences the macroscopic friction only when finite deformation effects accompany asperity interaction. In fact, for very low contact pressures ($\bar{t}_N \to 0$), the macroscopic friction coefficient $\bar{\mu}$ tends to the local friction coefficient μ_0 ($\bar{\mu} \to \mu_0$) so that friction at the macroscale is trivially governed by the local isotropic Coulomb friction model. Nontrivial effects are related to nonzero slope of asperity contacts which may only occur for sufficiently high contact pressures. Clearly, this concerns only elastic contacts, as considered in this work, and the above conclusion would not apply if inelastic deformation mechanisms (viscoelasticity, plasticity, etc.) were present in the surface layer or if another friction law was assumed to govern contact at the microscale.

Orientation- and pressure-dependence of the macroscopic friction coefficient, discussed in detail above, does not fully characterize the macroscopic friction model. Of interest is also the macroscopic slip rule which has been analyzed by comparing the actual angle $\delta = \alpha - \beta$ resulting from the micromechanical scheme to the one that would be observed for the associated macroscopic slip rule, see Fig. 10. The former is easily obtained by processing the results of finite element computations. The latter has been obtained by introducing an approximate polar representation $f(\alpha)$ of the macroscopic friction condition according to Eq. (8) and by applying Eq. (10) with $g(\alpha) = f(\alpha)$ that corresponds to the associated slip rule. Specifically, the numerically obtained dependence $\bar{\mu}(\alpha)$ has been fitted using the following function,

$$f(\alpha) = f_0 + \sum_{k=1}^{N} f_k \cos(2k\alpha), \tag{21}$$

with $N = 3$ (it has been checked that increasing the number of terms does not change the result visibly). As the macroscopic

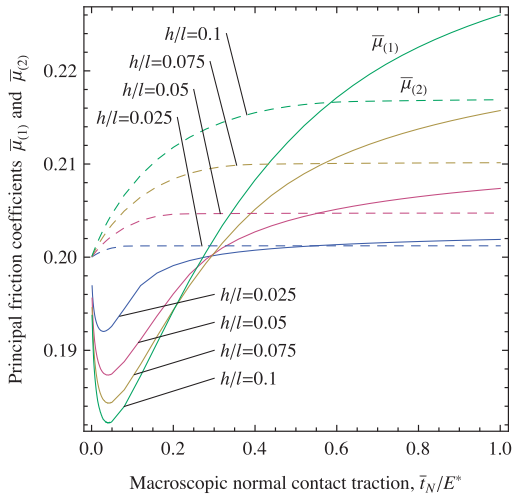

Fig. 9. Principal friction coefficients $\bar{\mu}_{(1)}$ (solid lines) and $\bar{\mu}_{(2)}$ (dashed lines) as a function of dimensionless normal contact traction $\bar{t}_N/E^*$ for $\nu = 0$ and $\mu_0 = 0.2$.

friction coefficient is pressure dependent, this procedure has been repeated for each value of contact pressure.

The results presented in Fig. 10 indicate that the macroscopic slip rule is a *non-associated* one, though non-associativity is not much pronounced. In fact, the actual angle δ is close to the one corresponding to the associated slip rule, and the difference is small and is below 1 degree in all analyzed cases (i.e., also for ν equal to -0.4, 0 and 0.25; the corresponding results are not reported here). As the difference is small, a careful mesh convergence study has been performed which confirmed that the observed departure from associativity is not a numerical artefact.

Recall that the slip rule at the microscale is an associated one hence the visible non-associativity of the macroscopic slip rule results from nonlinear effects accompanying asperity interaction and is revealed by micromechanical averaging. The same qualitative effect, though more pronounced, results also from the simple micromechanical model of Mróz and Stupkiewicz (1994). We believe that confirmation of this *qualitative* effect constitutes one of the main results of the present paper. Quantitatively, the effect is small, hence an associated slip rule may be a sufficiently good approximation in practice.

4.2. Randomly rough surfaces: isotropic roughness

Although the present paper is focused on friction anisotropy, the case of two isotropic randomly rough surfaces is considered in this section as a reference for the anisotropic case that is studied in the next section. However, the results of the corresponding micromechanical analysis are interesting themselves: it will be shown that some effects observed in the previous section for the idealized sinusoidal roughness are observed also for randomly rough isotropic surfaces.

Randomly rough surfaces have been generated using the random-field model, see Torquato (2002), extended to non-isotropic rough surfaces by Temizer (2011). The adopted procedure is briefly summarized below. First, an initial $N_x \times N_y$ matrix of roughness heights $g_{ij}^{(0)}$ with a Gaussian distribution is generated. The sequence of N_s smoothing operations with the periodic filter $\mathcal{F}$ is then performed,

$$g_{ij}^{(k)} = \mathcal{F}(g_{ij}^{(k-1)}) = \sum_{p=-r}^{r} \sum_{q=-r}^{r} g_{(i+p)(j+q)}^{(k-1)} \mathcal{K}(p,q), \quad k = 1, \ldots, N_s, \tag{22}$$

where $\mathcal{K}(p,q)$ is an anisotropic kernel,

$$\mathcal{K}(p,q) = \mathrm{Exp}\left(-(p'/a)^2 - (q'/b)^2\right), \quad (p',q') = \begin{bmatrix} \cos\theta & -\sin\theta \\ \sin\theta & \cos\theta \end{bmatrix} \begin{bmatrix} p \\ q \end{bmatrix}. \tag{23}$$

Here, the ratio a/b refers to the magnitude of anisotropy, and the angle θ describes the orientation of anisotropy axis with respect to the global axes. The special case of isotropy corresponds to $a = b$. The smoothed roughness $g_{ij}^{(N_s)}$ is then normalized so that the matrix g_{ij} of zero mean value and unit standard deviation is obtained, and a periodic $(N_x + 1) \times (N_y + 1)$ matrix of roughness heights $\bar{g}_{ij}$ is subsequently constructed by appending a copy of the first row and the first column to the respective end of the original matrix g_{ij}.

Isotropic roughness samples used in the present study have been generated according to the procedure described above using the following parameters: $N_x = N_y = 180$, $N_s = 6$, $r = 6$, and $a = b = 9$. These parameters have been selected by trial and error so that the roughness sample covers several asperities, say, 3–4 primary asperities along the sample edge. Of course, a larger

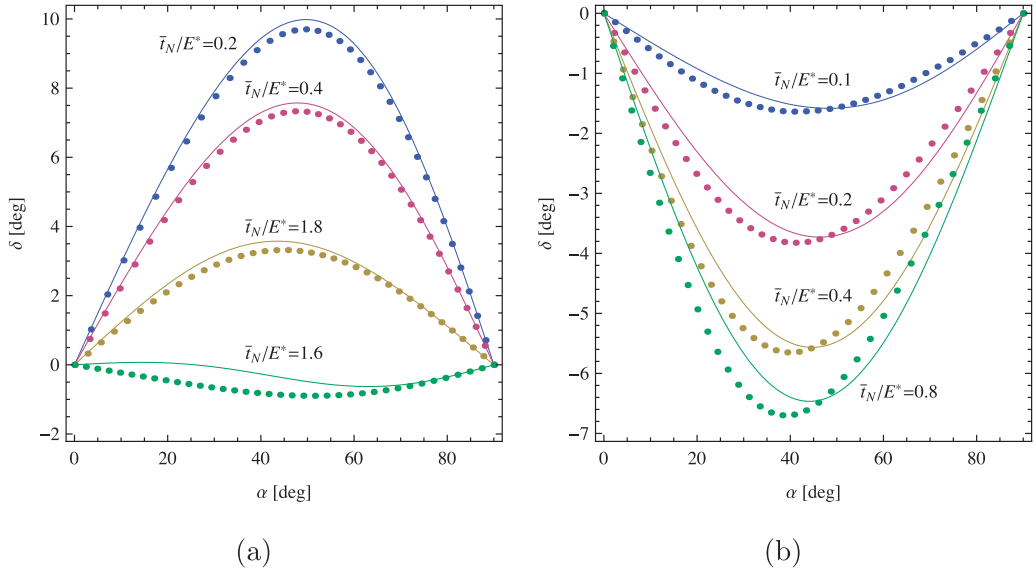

Fig. 10. Comparison of the actual angle $\delta = \alpha - \beta$ (indicated by the dots) and the one that would be observed if the macroscopic slip rule was an associated one (solid lines) for: (a) $\nu = -0.8$ and (b) $\nu = 0.45$.

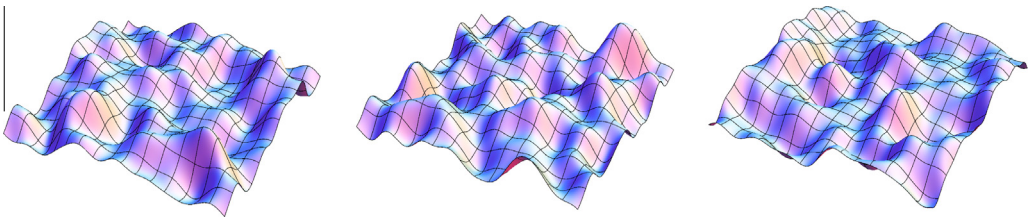

Fig. 11. Three isotropic roughness samples used in the computations. The height is scaled by the factor of five.

sample would be desirable, but the corresponding computational cost would be prohibitive, see the discussion below.

The actual finite element mesh used in the computations is coarser than the generated array of roughness heights, hence the positions of the finite element nodes of the contact surface are obtained by mapping the fine roughness topography to the coarser finite element mesh (Temizer, 2011). When generating the finite element mesh, the roughness heights have been finally scaled such that the ratio of the standard deviation of roughness heights to the sample size is equal to 0.01. Fig. 11 shows three samples of generated isotropic rough surfaces. Note that asperity height in Fig. 11 has been scaled by the factor of five for better visualization.

In the present computations, statistically identical roughness has been prescribed for both contact surfaces. Specifically, an isotropic roughness sample has been randomly generated for each surface independently, and the microscopic problem has been solved for the corresponding pair of roughness topographies. This has been repeated for other pairs of roughness topographies, and the macroscopic response has then been obtained by averaging over the ensemble. In the computations reported below, ten such samples have been analyzed for each value of the Poisson's ratio and for each value of the normal contact traction.

In the present microscopic problem, the bottom surface is assumed to be rigid, and the unit cell of the deformable upper surface is slid against the bottom surface by prescribing the displacements at the upper boundary Γ_l. The normal displacement at Γ_l is constant during the dragging phase so that the macroscopic normal contact traction is obtained by averaging the corresponding nodal reaction forces, see Section 3. The local friction coefficient is assumed as $\mu_0 = 0.2$.

Compared to the two-dimensional example of the previous section, the present case of two randomly rough surfaces is associated with a much higher computational cost. This is because, in addition to spacial averaging, also time averaging and ensemble averaging must be performed, see Section 3. The achievable resolution of the present three-dimensional finite-element model is thus

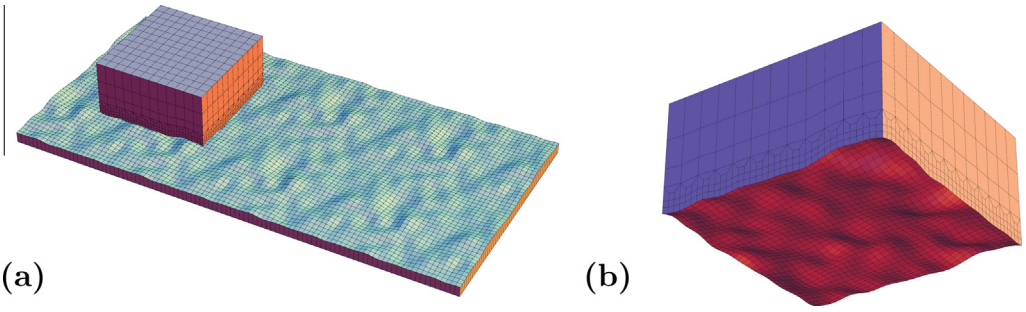

Fig. 12. Randomly rough surfaces in sliding contact: (a) overall view of the finite element mesh (the bottom surface is rigid) and (b) detailed view of the upper body (periodic unit cell of deformable surface layer).

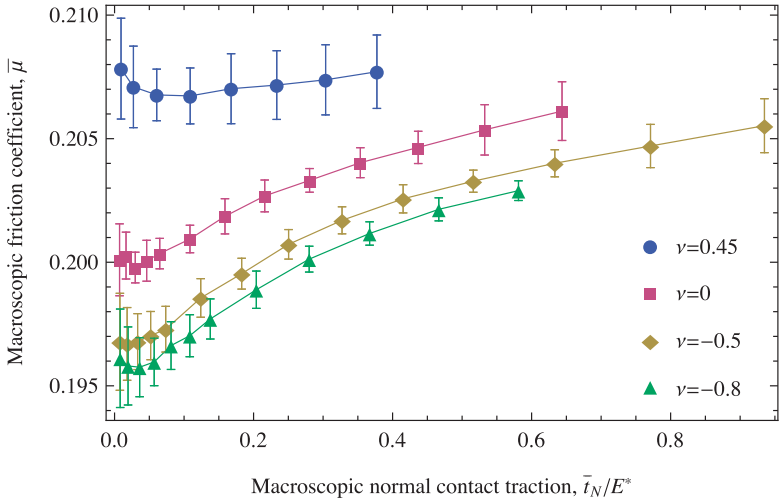

Fig. 13. Randomly rough isotropic surfaces: macroscopic friction coefficient $\bar{\mu}$ as a function of dimensionless macroscopic normal contact traction $\bar{t}_N/E^*$.

significantly constrained by the overall computational cost. Even though the actual mesh is relatively coarse, the present computations yield consistent results, as illustrated below.

The finite element mesh used in the computations is shown in Fig. 12. The bottom surface is periodically extended along the sliding direction. It is also extended transversally to accommodate 3D deformations of the unit cell. Contact smoothing is applied to the bottom surface using bicubic Bézier patches with 16-node support (Pietrzak, 1997), see also Lengiewicz et al. (2011). The mesh comprises about 16,500 displacement unknowns and about 4,000 contact Lagrange multipliers. The third phase of the microscopic problem requires 20–90 time increments (adaptive time stepping is used) depending on the contact pressure, Poisson's ratio and roughness sample.

Fig. 13 shows the macroscopic friction coefficient $\bar{\mu}$ as a function of the dimensionless normal contact traction $\bar{t}_N/E^*$ and the Poisson's ratio ν. The markers denote the ensemble average, and the error bars indicate the standard deviation of the friction coefficients computed for individual roughness samples.

The results confirm two effects that have been observed for the sinusoidal roughness in Section 4.1. The macroscopic friction coefficient $\bar{\mu}$ decreases with decreasing Poisson's ratio and it may be lower than the local friction coefficient $\mu_0 = 0.2$. In fact, the results reported in Fig. 13 are similar to those reported in Fig. 8. The main qualitative difference is that the macroscopic friction coefficient $\bar{\mu}$ does not seem to tend to the local friction coefficient μ_0 as the contact pressure tends to zero, in particular, for the nearly incompressible material ($\nu = 0.45$). This probably results from insufficient resolution of the finite element model. Note that a very fine mesh was needed to reproduce that effect in the case of sinusoidal roughness in Section 4.1.

4.3. Randomly rough surfaces: anisotropic roughness

In this section, the example of the previous section is modified by adopting an anisotropic roughness for the bottom, rigid surface. All the other details of the computational model are unaltered, including the finite element mesh shown in Fig. 12 and local friction coefficient $\mu_0 = 0.2$.

Fig. 14 shows three samples of the anisotropic roughness generated following the procedure described in the previous section. Application of the anisotropic filter with parameters $k = 6, r = 20, a = 5, b = 20$ and $\theta = 90^\circ$ results now in elongated asperities with clearly visible preferential direction. At the same time, roughness of the upper surface is assumed isotropic, as in Fig. 11. As a result, friction at the macroscale is expected to exhibit orthotropic symmetry with two principal directions corresponding to sliding across and along the elongated asperities of the bottom surface. The corresponding principal macroscopic friction coefficients have been computed for a nearly incompressible material ($\nu = 0.45$) and for a compressible auxetic material ($\nu = -0.8$).

The results are reported in Fig. 15. As previously, the error bars indicate the standard deviation of the friction coefficients computed for individual roughness samples. Note that convergence problems have been encountered at higher contact pressures for $\nu = 0.45$ and $\beta = 0$ (sliding across the elongated asperities), hence the corresponding two points are missing in Fig. 15.

As previously, the results shown in Fig. 15 confirm the effects observed for the idealized sinusoidal roughness in Section 4.1. In the case of a nearly incompressible material ($\nu = 0.45$), the macroscopic friction coefficient corresponding to sliding across the elongated asperities ($\beta = 0$) is higher than that corresponding to sliding along the asperities ($\beta = 90^\circ$). At the same time, the effect is

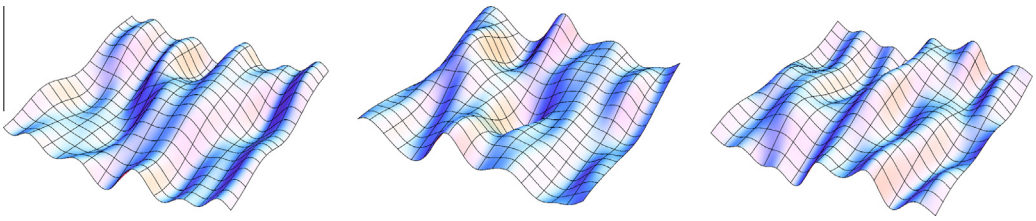

Fig. 14. Three anisotropic roughness samples used in the computations. The height is scaled by the factor of five.

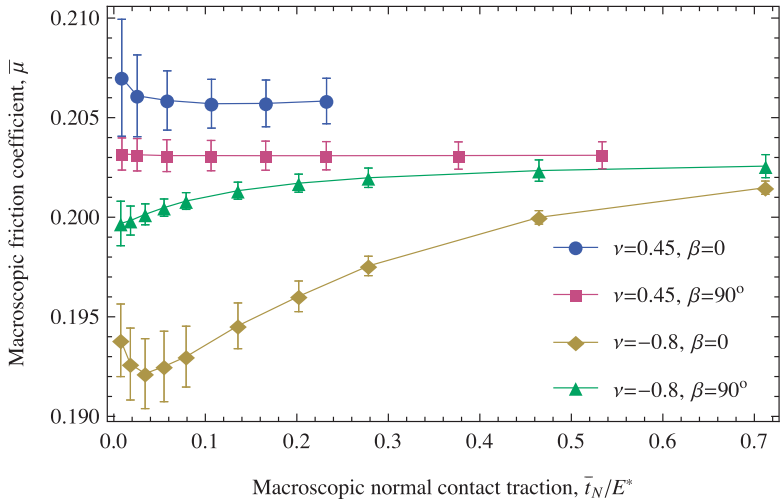

Fig. 15. Anisotropic roughness: macroscopic friction coefficient $\bar{\mu}$ as a function of dimensionless macroscopic normal contact traction $\bar{t}_N/E^*$ for $\beta = 0$ (sliding across the elongated asperities) and $\beta = 90^\circ$ (sliding along the elongated asperities).

reversed in the case of the compressible (auxetic) material ($\nu = -0.8$). Also, it is seen that the macroscopic friction coefficient decreases with decreasing Poisson's ratio, and it may be lower than the local friction coefficient μ_0.

5. Conclusion

Friction anisotropy resulting from asperity interaction in rough elastic contacts has been studied using the computational contact homogenization approach with full account for finite deformation effects. Friction at local contacts has been assumed to be the only dissipative mechanism in the system. The study is thus only concerned with the effect of anisotropic roughness on macroscopic friction of elastic bodies. While the adopted micromechanical framework can be considered rather standard, a micromechanical study of such a scope has not been reported in the literature yet.

The influence of local friction coefficient, asperity height, and elastic compressibility on friction anisotropy has been studied in detail in the case of contact of a smooth hyperelastic half-space with a rigid surface with sinusoidal roughness. As the corresponding microscopic problem is a two-dimensional steady-state problem, a highly accurate finite element model could have been developed for that case. The effects predicted for the idealized sinusoidal roughness have been confirmed by the results obtained for a more general case of contact of two randomly rough surfaces. The latter case is computationally much more demanding as it involves solution of several three-dimensional transient contact problems followed by averaging over an ensemble.

The results of the present study confirm that roughness anisotropy leads to anisotropy of friction at the macroscale, i.e., to an orientation-dependent macroscopic friction coefficient. For the roughness topographies considered in this work, the macroscopic friction is actually orthotropic. The macroscopic friction coefficient is also found to depend on the contact pressure, which is expected since the average asperity slope depends on the contact pressure. In fact, nontrivial effects are only observed for relatively high contact pressures because, for the contact pressure close to zero, the surfaces interact at practically undeformed asperity tops, and the local isotropic Coulomb friction model is valid also at the macroscale.

It has been also found that the macroscopic friction condition is accompanied by a non-associated slip rule, though the non-associativity is not much pronounced (it is recalled that associativity refers here only to the tangent plane). Note that the slip rule at the microscale is an associated one; the associativity is thus not transmitted to the macroscale. The predicted non-associativity of the macroscopic slip rule results from nonlinear effects accompanying asperity interaction at the microscale. This effect is in a qualitative agreement with the simple model of Mróz and Stupkiewicz (1994).

The results of the present micromechanical study show a significant effect of material compressibility. For a nearly incompressible material, the macroscopic friction coefficient is higher than the local friction coefficient. Further, in case of anisotropic roughness, sliding across elongated asperities results in a higher friction than sliding along them. However, with increasing compressibility (i.e., with decreasing Poisson's ratio), both effects are gradually reversed. Those counterintuitive effects are particularly pronounced for auxetic materials, i.e., for a negative Poisson's ratio.

Acknowledgement

This work has been partially supported by the National Science Centre (NCN) in Poland under Grant No. 2011/01/B/ST8/07434.

References

Alart, P., Curnier, A., 1991. A mixed formulation for frictional contact problems prone to Newton like solution methods. Comput. Methods Appl. Mech. Eng. 92, 353–375.
Anciaux, G., Molinari, J.F., 2010. Sliding of rough surfaces and energy dissipation with a 3D multiscale approach. Int. J. Numer. Methods Eng. 83, 1255–1271.
Bandeira, A.A., Wriggers, P., Pimenta, P.D., 2004. Numerical derivation of contact mechanics interface laws using a finite element approach for large 3D deformation. Int. J. Numer. Methods Eng. 59, 173–195.
Bertoldi, K., Bigoni, D., Drugan, W.J., 2007. Structural interfaces in linear elasticity. Part I: nonlocality and gradient approximations. J. Mech. Phys. Solids 55, 1–34.
Buczkowski, R., Kleiber, M., 2006. Elasto-plastic statistical model of strongly anisotropic rough surfaces for finite element 3d-contact analysis. Comput. Methods Appl. Mech. Eng. 195, 5141–5161.
Carbone, G., Lorenz, B., Persson, B.N.J., Wohlers, A., 2009. Contact mechanics and rubber friction for randomly rough surfaces with anisotropic statistical properties. Eur. Phys. J. E 29, 275–284.
Casey, M., Wilks, J., 1973. The friction of diamond sliding on polished cube faces of diamond. J. Phys. D: Appl. Phys. 6, 1772–1781.
Curnier, A., 1984. A theory of friction. Int. J. Solids Struct. 20, 637–647.
De Lorenzis, L., Wriggers, P., 2013. Computational homogenization of rubber friction on rough rigid surfaces. Comput. Mater. Sci. 77, 264–280.
de Souza Neto, E.A., Perić, D., Dutko, M., Owen, D.R.J., 1996. Design of simple low order finite elements for large strain analysis of nearly incompressible solids. Int. J. Solids. Struct. 33, 3277–3296.
Greenwood, J.A., Williamson, J.B.P., 1966. Contact of nominally flat surfaces. Proc. R. Soc. Lond. A 295, 300–319.
Hazel, J., Stone, M., Grace, M.S., Tsukruk, V.V., 1999. Nanoscale design of snake skin for reptation locomotions via friction anisotropy. J. Biomech. 32, 477–484.
He, Q.C., Curnier, A., 1993. Anisotropic dry friction between 2 orthotropic surfaces undergoing large displacements. Eur. J. Mech. A/Solids 12, 631–666.
Hill, R., Rice, J.R., 1973. Elastic potentials and the structure of inelastic constitutive laws. SIAM J. Appl. Math. 25, 448–461.
Hirano, M., Shinjo, K., 1993. Superlubricity and frictional anisotropy. Wear 168, 121–125.
Hjiaj, M., Feng, Z.Q., de Saxcé, G., Mróz, Z., 2004. On the modelling of complex anisotropic frictional contact laws. Int. J. Eng. Sci. 42, 1013–1034.
Hjiaj, M., Feng, Z.Q., de Saxcé, G., Mróz, Z., 2004. Three-dimensional finite element computations for frictional contact problems with non-associated sliding rule. Int. J. Numer. Methods. Eng. 60, 2045–2076.
Jones, R.E., Papadopoulos, P., 2006. Simulating anisotropic frictional response using smoothly interpolated traction fields. Comput. Methods. Appl. Mech. Eng. 195, 588–613.
Konyukhov, A., Schweizerhof, K., 2006. Covariant description of contact interfaces considering anisotropy for adhesion and friction: part 2. Linearization, finite element implementation and numerical analysis of the model. Comput. Methods. Appl. Mech. Eng. 196, 289–303.
Konyukhov, A., Vielsack, P., Schweizerhof, K., 2008. On coupled models of anisotropic contact surfaces and their experimental validation. Wear 264, 579–588.
Korelc, J., 2002. Multi-language and multi-environment generation of nonlinear finite element codes. Eng. Comput. 18, 312–327.
Korelc, J., 2009. Automation of primal and sensitivity analysis of transient coupled problems. Comput. Mech. 44, 631–649.
Laursen, T.A., 2002. Computational Contact and Impact Mechanics. Springer-Verlag, Berlin.
Le Quang, H., He, Q.C., Le, H.T., 2013. Multiscale homogenization of elastic layered composites with unidirectionally periodic rough interfaces. SIAM Multiscale Model. Simul. 11, 1127–1148.
Lengiewicz, J., Korelc, J., Stupkiewicz, S., 2011. Automation of finite element formulations for large deformation contact problems. Int. J. Numer. Methods. Eng. 85, 1252–1279.
Majumdar, A., Bhushan, B., 1991. Fractal model of elastic–plastic contact between rough surfaces. Trans. ASME J. Tribol. 113, 1–11.
Michałowski, R., Mróz, Z., 1978. Associated and non-associated sliding rules in contact friction problems. Arch. Mech. 30, 259–276.
Mróz, Z., Stupkiewicz, S., 1994. An anisotropic friction and wear model. Int. J. Solids Struct. 31, 1113–1131.
Murphy, M., Aksak, B., Sitti, M., 2007. Adhesion and anisotropic friction enhancements of angled heterogeneous micro-fiber arrays with spherical and spatula tips. J. Adhes. Sci. Technol. 21, 1281–1296.
Nemat-Nasser, S., Hori, M., 1999. Micromechanics: Overall Properties of Heterogeneous Materials. Elsevier, Amsterdam.
Orlik, J., 2004. Homogenization for Contact Problems with Periodically Rough Surfaces. Tech. Rep., Fraunhofer Institut Techno- und Wirtschaftsmathematik, Kaiserslautern, Germany.
Ozaki, S., Hikida, K., Hashiguchi, K., 2012. Elastoplastic formulation for friction with orthotropic anisotropy and rotational hardening. Int. J. Solids. Struct. 49, 648–657.
Pei, L., Hyun, S., Molinari, J.F., Robbins, M.O., 2005. Finite element modelling of elasto-plastic contact between rough surfaces. J. Mech. Phys. Solids 53, 2385–2409.
Persson, B.N.J., 2001. Theory of rubber friction and contact mechanics. J. Chem. Phys. 115, 3840–3861.

Petryk, H., Stupkiewicz, S., Maciejewski, G., 2010. Interfacial energy and dissipation in martensitic phase transformations. Part II: size effects in pseudoelasticity. J. Mech. Phys. Solids 58, 373–389.

Pietrzak, G., 1997. Continuum mechanics modelling and augmented Lagrangian formulation of large deformation frictional contact problems (Ph.D. thesis). Lausanne, EPFL.

Pietrzak, G., Curnier, A., 1999. Large deformation frictional contact mechanics: continuum formulation and augmented Lagrangian treatment. Comput. Methods Appl. Mech. Eng. 177, 351–381.

Qu, J., Cherkaoui, M., 2006. Fundamentals of Micromechanics of Solids. John Wiley & Sons Inc, Hoboken, New Jersey.

Rodriguez-Tembleque, L., Abascal, R., 2013. Fast FE–BEM algorithms for orthotropic frictional contact. Int. J. Numer. Methods Eng. 94, 687–707.

Sadowski, P., Stupkiewicz, S., 2010a. Combined effect of friction and macroscopic deformation on asperity flattening. Tribol. Int. 43, 1735–1741.

Sadowski, P., Stupkiewicz, S., 2010b. A model of thermal contact conductance at high real contact area fractions. Wear 268, 77–85.

Spijker, P., Anciaux, G., Molinari, J.F., 2013. Relations between roughness, temperature and dry sliding friction at the atomic scale. Tribol. Int. 59, 222–229.

Stupkiewicz, S., 2007. Micromechanics of Contact and Interphase Layers. Springer, Berlin Heidelberg New York.

Stupkiewicz, S., Maciejewski, G., Petryk, H., 2007. Low-energy morphology of the interface layer between austenite and twinned martensite. Acta Mater. 55, 6292–6306.

Sung, N.H., Suh, N.P., 1979. Effect of fiber orientation on friction and wear of fiber reinforced polymeric composites. Wear 53, 129–141.

Temizer, I., 2011. Thermomechanical contact homogenization with random rough surfaces and microscopic contact resistance. Tribol. Int. 44, 114–124.

Temizer, I., Wriggers, P., 2008. A multiscale contact homogenization technique for the modelling of third bodies in the contact interface. Comput. Methods Appl. Mech. Eng. 198, 377–396.

Temizer, I., Wriggers, P., 2010. Inelastic analysis of granular interfaces via computational contact homogenization. Int. J. Numer. Methods Eng. 84, 883–915.

Torquato, S., 2002. Random Heterogeneous Materials: Microstructure and Macroscopic Properties. Springer, Berlin Heidelberg New York.

Varadi, K., Neder, Z., Friedrich, K., 1996. Evaluation of the real contact areas, pressure distributions and contact temperatures during sliding contact between real metal surfaces. Wear 200, 55–62.

Vinh, P.A., Tung, D.X., 2012. Explicit homogenized equation of a boundary-value problem in two-dimensional domains separated by an interface highly oscillating between two concentric ellipses. Arch. Mech. 64, 461–476.

Wriggers, P., 2006. Computational Contact Mechanics, 2nd Edition. Springer, Berlin Heidelberg New York.

Wriggers, P., Reinelt, J., 2009. Multi-scale approach for frictional contact of elastomers on rough rigid surfaces. Comput. Methods Appl. Mech. Eng. 198, 1996–2008.

Zhang, H., Komvopoulos, K., 2009. Scale-dependent nanomechanical behavior and anisotropic friction of nanotextured silicon surfaces. J. Mater. Res. 24, 3039–3043.

Zhang, Q.S., Chen, X.B., Yang, Q., Zhang, W.J., 2012. Development and characterization of a novel piezoelectric-driven stick-slip actuator with anisotropic-friction surfaces. Int. J. Adv. Manuf. Technol. 61, 1029–1034.

Zmitrowicz, A., 1989. Mathematical descriptions of anisotropic friction. Int. J. Sol. Struct. 25, 837–862.